

## LENSING-INDUCED CLUSTER SIGNATURES IN THE COSMIC MICROWAVE BACKGROUND

UROŠ SELJAK

Department of Physics, Jadwin Hall, Princeton University, Princeton, NJ 08544

AND

MATIAS ZALDARRIAGA

Institute for Advanced Studies, School of Natural Sciences, Princeton, NJ 08540

Received 1999 July 21; accepted 2000 February 28

### ABSTRACT

We show that clusters of galaxies induce steplike wiggles on top of the cosmic microwave background (CMB). The direction of the wiggle is parallel to the large-scale gradient of the CMB, allowing one to isolate the effect from other small-scale fluctuations. The effect is sensitive to the deflection angle rather than its derivative (shear or magnification) and thus traces outer parts of the cluster with higher sensitivity than some other methods. A typical amplitude of the effect is  $10 \mu\text{K}(\sigma_v/1400 \text{ km s}^{-1})^2$ , where  $\sigma_v$  is the velocity dispersion of the cluster, and several  $\mu\text{K}$  signals extend out to a fraction of a degree. We derive the expressions for the temperature profile for several simple parameterized cluster models and identify some degeneracies between parameters. Finally, we discuss how to separate this signal from other imprints on the CMB using custom-designed filters. Detection of this effect is within reach of the next generation of small-scale CMB telescopes and could provide information about the cluster density profile beyond the virial radius.

*Subject headings:* cosmic microwave background — gravitational lensing — large-scale structure of universe

### 1. INTRODUCTION

Fluctuations in the cosmic microwave background (CMB) are believed to originate from the era of hydrogen recombination at a redshift of  $z \sim 1100$ . Before recombination, photons and electrons were tightly coupled via the process of Thomson scattering, while afterward electrons were bound to protons in hydrogen and photons were allowed to propagate freely through the universe. Already before and especially during recombination the coupling was not perfect, leading to erasure of fluctuations in the CMB on small scales. As a result, these primary fluctuations are expected to be very smooth on scales below  $10'$ .

On very small scales, the CMB can be considered as a simple gradient. A mass concentration in front of such a gradient gravitationally deflects the light. This deflection causes a fluctuation in the CMB temperature, which is determined by the mapping between unperturbed and perturbed photon position (see also A. Kosowsky et al. in preparation). This additional fluctuation is preferentially generated in the regions of high gradient of primary CMB anisotropies. The effect can be generated by any mass concentrations along the line of sight, such as galaxy halos, clusters, and superclusters. In this paper we concentrate on clusters, which, being massive and large, may generate a particularly strong effect. They are thus the primary candidates for detection of this effect on individual objects, as opposed to the statistical detection discussed in Zaldarriaga & Seljak (1999) and Zaldarriaga (1999). The purpose of this paper is to analyze their imprint on the microwave sky by analyzing a number of simple cluster profiles and to discuss its detectability for realistic observational scenarios. The main feature of this effect is that it is sensitive to the photon deflection angle and not its derivative, as in the case of shear or magnification measurements of background galaxies (see Mellier 1999 for a review). The deflection angle decreases less rapidly away from the cluster center than other tracers,

so this method potentially provides sensitivity to cluster detection at large radii.

It should be stressed that this gravitational lensing effect is different from the lensing effect of a cluster as discussed in Zaldarriaga & Seljak (1999). There, the CMB was viewed as a collection of peaks, with a well-determined distribution of shapes and sizes in Gaussian models. These will be distorted as they pass by a large massive object, generating a coherent ellipticity or size distortion that can be identified by averaging over a sufficient number of independent patches. By averaging over the CMB, the lensing effect can be isolated and a cluster density profile can be reconstructed Zaldarriaga & Seljak (1999). In practice, this requires the presence of small-scale CMB fluctuations at detectable levels, and these are not likely to originate from primary anisotropies. Secondary processes and foregrounds reviewed in this paper could provide the small-scale power required, although the level of these small-scale fluctuations is still uncertain at present. In principle, this would provide an alternative method for reconstructing the cluster density profile, in addition to the one discussed here. Given the uncertain level of secondary anisotropies, in the remainder of this paper we will ignore this possibility, adopting a conservative position that secondary anisotropies are only a source of confusion to the signal one is trying to isolate.

### 2. LENSING EFFECT OF CLUSTERS ON THE CMB

The measured temperature field,  $T(\theta)$ , at observed position  $\theta$  originates from some unlensed position  $\theta'$  of the CMB field at the last scattering surface,  $\tilde{T}(\theta')$ . The relation between the two is given through the deflection angle of the CMB photons,  $\delta\theta$ ;

$$\begin{aligned} T(\theta) &= \tilde{T}(\theta') = \tilde{T}(\theta - \delta\theta) \\ &\approx \tilde{T}(\theta) - \delta\theta \cdot \nabla \tilde{T}(\theta) . \end{aligned} \quad (1)$$

In the second line, we expanded the temperature using a linear expansion valid on scales below the coherence length of the CMB gradient, which is of the order of  $15'$  for typical models in a flat universe. On scales below that, the primary anisotropies are expected to have negligible power. In this case, we can treat the unlensed temperature field as a pure gradient. We are ignoring all the secondary anisotropies and foregrounds generated along the line of sight that will contribute to fluctuations on these small scales. These act as a source of noise and are discussed later in the paper.

We choose  $\theta = (\theta_x, \theta_y) = (\theta \cos \phi_\theta, \theta \sin \phi_\theta)$  to be the observed position in the sky, with origin at the cluster center. The derivative of the deflection angle with respect to  $\theta$  is the shear tensor, which can be decomposed into its trace part,  $2\kappa$ , and two shear components,  $\gamma_1$  and  $\gamma_2$ . The convergence,  $\kappa$ , is dimensionless and can be expressed in terms of projected density,  $\Sigma$ , as  $\kappa = \Sigma/\Sigma_{\text{cr}}$ , where

$$\Sigma_{\text{cr}} = \frac{c^2 D_{OS}}{4\pi G D_{OL} D_{LS}},$$

where  $D_{LS}$  is the angular diameter distance from the lens to the source,  $D_{OS}$  between the observer and the source, and  $D_{OL}$  between observer and lens. We can parameterize the density profile of the cluster in units of a characteristic length scale,  $r_s$ , as  $\rho(x)$ , where  $x = r/r_s$  and  $r$  is the radius. When we measure angles in units of  $\theta_s = r_s/D_{OL}$ , so that  $x = r/r_s = \theta/\theta_s$ , and the deflection angle scales as  $\delta\theta \propto m(x)/x$ , where  $m(x)$  is the mass enclosed within the projected radius  $x$ .

Without a loss of generality, we can take the gradient to be along the  $y$  axis with an amplitude  $\tilde{T}_{y0}$ . The observed temperature then becomes

$$T(\theta) = \tilde{T}_{y0}(\theta_y - \delta\theta_y). \quad (2)$$

In the absence of deflection,  $\delta\theta_y$ , one would measure a pure gradient. Any small-scale deviation from it is a signature of the deflection,  $\delta\theta_y$ . If we measure the value of the large-scale gradient by filtering out small scales contaminated by the cluster lensing, we would know where a certain value of the CMB anisotropy should have come from in the absence of deflection. The difference between the expected and measured position is a direct measurement of  $\delta\theta_y$ , and so of the gravitational effect of the cluster. The effect on the CMB of lensing by a cluster can be understood with the help of Figure 1. In the absence of lensing, we would observe just the gradient. Because of the lensing effect by the cluster, the light rays will be deflected radially, so that for  $\theta_y > 0$  the rays are coming from a lower value of  $\theta_y$  at the last scattering surface. If the gradient is positive, this implies that for  $\theta_y > 0$ , in the presence of the cluster we would observe a lower temperature than what would be observed if the cluster was not there. The opposite is true for  $\theta_y < 0$ . Far away from the cluster, the lensed temperature should again coincide with the gradient. Thus, the cluster creates a wiggle on top of the large-scale gradient.

It is important to stress that the method proposed here is sensitive to one component of the deflection angle and not the shear or magnification, as is the case for the usual weak-lensing reconstruction from background galaxy ellipticities or magnitudes. It is sometimes argued that we can never measure the deflection angle in a lensing system because we do not know the original position of the background image. In this case, we can get around this argument because we

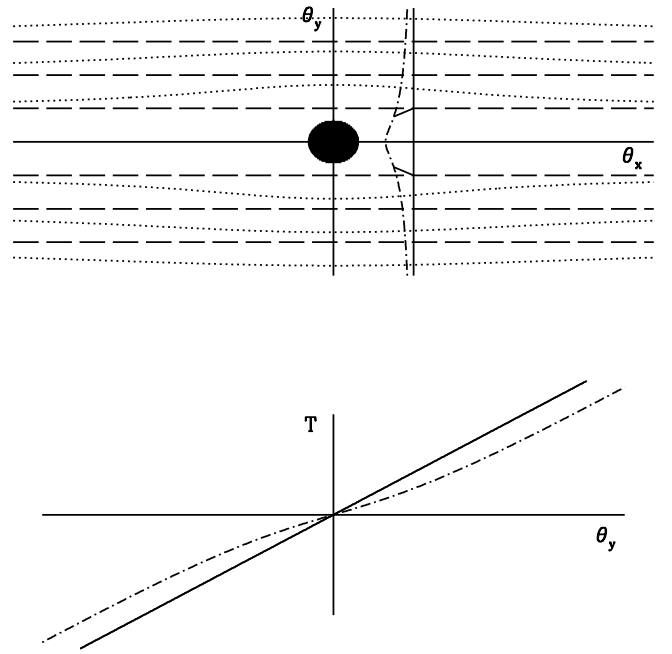


FIG. 1.—*Top*: Cluster lensing a background gradient. Dashed and dotted lines show isotherm contours before and after lensing, respectively. The displacement is radial, and a photon observed along the fixed  $\theta_x$  direction (solid line) is originating from a different position (dash-dotted line). *Bottom*: Temperature measured at a fixed  $\theta_x$  as a function of  $\theta_y$  before (solid) and after (dash-dotted line) the cluster lensing. Points with  $\theta_y > 0$  are deflected to a smaller  $\theta_y$  in the lens plane, and thus for a positive gradient they will have a lower temperature when the cluster is present. The opposite is true if  $\theta_y < 0$ .

know that the background image is a gradient that we can measure on scales larger than the cluster. Although both shear and deflection angle are sensitive to the cluster mass profile, the latter involves one derivative of gravitational potential less than the former. As such, it is less sensitive to small-scale fluctuations in the cluster profile and more sensitive to the outer parts of the cluster, as discussed below.

Another important point is that the effect discussed here is proportional to the gradient  $T_{y0}$ . This provides a unique signature that we can use to separate it from other sources of anisotropies. It also implies that one should select the clusters in which to look for this effect not only on the basis of the strength of the gravitational lensing signal, but also on the basis of the amplitude of the CMB gradient at that position. MAP or some other CMB experiment with  $15'$  resolution could provide such information.

### 2.1. Singular Isothermal Sphere

For a singular isothermal sphere, the density scales as  $\rho \propto r^{-2}$ . In this case, the deflection angle is constant,

$$\delta\theta_y = b \frac{\theta_y}{\theta}, \quad (3)$$

where  $b = 4\pi(\sigma_v/c)^2 D_{LS}/D_{OS} \sim 1'(\sigma_v/1400 \text{ km s}^{-1})^2 D_{LS}/D_{OS}$ , where  $\sigma_v$  is the cluster velocity dispersion. With the source at  $z \sim 1100$ , we can assume  $D_{OS} \gg D_{LS}$ , which in an Einstein–de Sitter universe gives  $D_{LS}/D_{OS} \approx 1/(1+z_L)^{1/2}$ .

The mass for a singular isothermal profile grows linearly with radius, but numerical simulations (Navarro, Frenk, & White 1997; NFW) show that at the outer parts, the profile

must turn over to a steeper slope. We will adopt the profile

$$\rho(x) \propto [x^2(1+x)]^{-1}, \quad (4)$$

where the slope in the outer parts of the cluster has been matched to the NFW profile discussed below. We have numerically integrated the equations above to compute the mass within a given radius and the deflection angle. These are shown together with the surface density  $\kappa$  in Figure 2, where it can be seen that  $\kappa$  is dropping with radius much more rapidly than  $\delta\theta$ .

In Figure 3, we show the signature of the effect on the CMB itself. We have subtracted out the gradient term. We focus on the temperature as a function of  $\theta_y$  for a fixed  $\theta_x$ . We adopt  $\sigma_v = 1400 \text{ km s}^{-1}$  and  $\theta_s = r_s/D_{OL} \sim 1.4$  (corresponding to A370; see Williams, Navarro, & Bartelmann 1999). The amplitude of the wiggle is  $T_{y0} \delta\theta$ , proportional to the amplitude of the gradient and the deflection angle. For  $\theta_x = 0$ , the distortion caused by a singular isothermal sphere (SIS) cluster would be constant and negative for  $\theta_y > 0$  and constant and positive for  $\theta_y < 0$ , with a step function at  $\theta_y = 0$ , reflecting the absence of a core in this model. The change in slope in the outer parts alters this prediction, so that only for  $\theta < \theta_s$  is the deflection angle approximately constant (Fig. 2). For  $\theta_x \neq 0$  the temperature profile is smooth, but the functional dependence still has odd symmetry with respect to the transformation across the  $y$ -axis, as shown in Figure 3a. The value for the distortion depends on the amplitude of the large-scale gradient, which has an rms value of  $\sigma_{\nabla T} = \langle T_x^2 + T_y^2 \rangle^{1/2}$ , of the order of  $13 \mu\text{K arcmin}^{-1}$  for standard cold dark matter (CDM). Other models that fit the current observations give similar values for  $\sigma_{\nabla T}$ . We have adopted this value of the gradient for our calculation, which gives a distortion  $\Delta T \sim b\sigma_{\nabla T} \sim 13 \mu\text{K}(\sigma_v/1400 \text{ km s}^{-1})^2 D_{LS}/D_{OS}$ . Note that  $\mu\text{K}$  signals can be obtained well beyond the virial radius, and that by averaging over the entire profile of the signal, one can significantly reduce the level of contamination from other contributions.

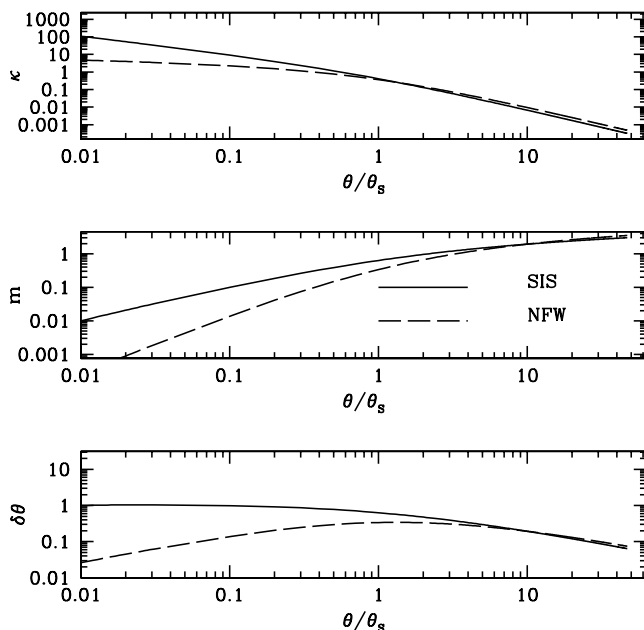


FIG. 2.—Dimensionless surface density  $\kappa$ , mass  $m$  within the projected distance, and deflection angle  $\delta\theta$  as a function of projected distance  $x = \theta/\theta_s$ . Solid lines show SIS and dashed lines NFW profiles.

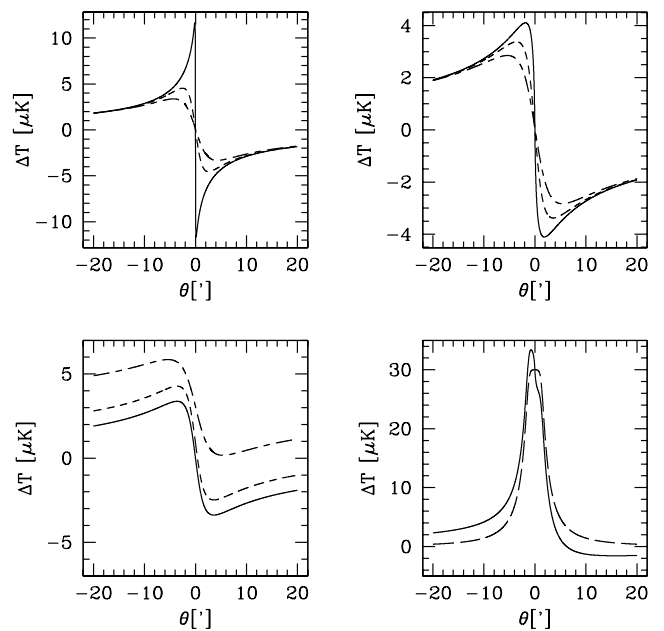


FIG. 3.—Temperature profile of a CMB gradient lensed by an SIS (top left) and NFW (top right) cluster at a fixed  $\theta_x$ . From top to bottom,  $\theta_x = 0'$ ,  $3'$ ,  $10'$ . The gradient part has been subtracted out for clarity. Bottom left shows the same profile for NFW with external shear, showing how the odd symmetry across the  $y$ -axis is broken for  $\theta_x \neq 0$ . Bottom right shows imprint of kinetic SZ (dashed line) and lensing effect and kinetic SZ superimposed (solid line). This also breaks the symmetry across the  $y$ -axis, but it is more concentrated in the center than the effect of external shear.

This is discussed in more detail in § 4, where we address more generally the observability of this signal.

## 2.2. NFW Profile

Navarro, Frenk, & White (1997; NFW) proposed a universal mass profile that was shown to fit most of the halos in cosmological  $N$ -body simulations. Its three-dimensional form is particularly simple, and is given by

$$\rho(x) = \frac{\rho_s}{x(1+x)^2}. \quad (5)$$

The transition between  $r^{-1}$  scaling in the center and  $r^{-3}$  outside is governed by the scale radius,  $r_s$ . Typical numbers for a cluster halo are of the order of  $250 h^{-1} \text{ kpc}$  for  $r_s$ , which is about 15%–20% of the virial radius,  $r_{200}$ , defined as the radius within which the mean overdensity is 200.

We numerically calculated the expected temperature profile for the parameters of A370, shown in Figure 3b. We normalized both SIS and NFW profiles to have the same total mass at large radii. Because of our choice of normalization, we see that the largest difference between the NFW and SIS profiles occurs near the core of the cluster, in the inner  $2'$ . The NFW profile has much less mass near the center and thus has a much smaller deflection angle. Arc-minute or better resolution is needed to distinguish these two profiles with this method. We will show below that other contributions, such as instrument noise, infrared (IR), or radio point sources, as well as Sunyaev-Zeldovich (SZ) scattering, further complicate this separation.

## 2.3. Nonaxisymmetric Profile

Let us now introduce a quadrupole deviation from axial symmetry in the form of external shear. This can be param-

eterized with two components: distortion along the  $x$ ,  $y$ -axis, parameterized with  $\gamma_1$ , and distortion along the diagonals, parameterized with  $\gamma_2$ . Fermat's gravitational potential can be parameterized in the form

$$\Phi = \frac{\delta\theta \cdot \delta\theta}{2} - f(\theta) - \frac{1}{2} \theta^2 (\gamma_1 \cos 2\phi_\theta + \gamma_2 \sin 2\phi_\theta), \quad (6)$$

where  $f(\theta)$  is a general function describing the axisymmetric (in angle) radial profile of the projected cluster potential. This can be expanded into a series  $f(\theta) = f_1 \theta + f_2 \theta^2/2 + \dots$

From Fermat's principle, we obtain

$$\delta\theta_y = \theta_y \left[ \gamma_1 - \frac{f'(\theta)}{\theta} \right] - \gamma_2 \theta_x. \quad (7)$$

Inserting the expansion of  $f$  above, we find that  $\gamma_1$  and  $f_2$  are degenerate, since  $\delta\theta_y$  has the same dependence on  $\theta$  for both parameters. This degeneracy is similar to the mass-sheet degeneracy that exists in the case of cluster reconstruction from the shear. In that case, a constant mass sheet cannot be detected using the shear information alone. Similarly, here we cannot separate between a constant mass sheet and an external shear component,  $\gamma_1$ . A more general form of this degeneracy is derived in the next section.

External shear distortion that is not perpendicular or parallel to the  $y$  axis can be measured from the profile. The case of  $\gamma_2 = 0.3$  and an NFW profile is shown in Figure 3c. Nonaxial symmetry breaks the odd parity symmetry across the  $y$ -axis for  $\theta_x \neq 0$ . At a given  $\theta_x$ , the whole wiggle is moved up or down depending on  $\gamma_2$  (of course, far away from the shear source it is restored back to the unperturbed value). This is not the only effect that can break this symmetry. As discussed in more detail in § 4, kinetic and thermal SZ effects also imprint a signal in the CMB. Kinetic SZ effects in particular cannot be distinguished from lensing or primary CMB on the basis of frequency dependence. For an axial-symmetric cluster, it produces a profile with even parity across the  $y$ -axis. This effect, combined with the lensing effect, also breaks the symmetry, as shown in Figure 3d. It is much more centrally concentrated than the effect of external shear, so that the two can be separated.

### 3. RECONSTRUCTION OF PROJECTED DENSITY

Rather than parameterizing the surface density of the cluster, one can also attempt to reconstruct it directly. To do this, we first subtract the pure gradient term from the CMB anisotropies and divide the temperature by  $T_{y0}$ . This gives an estimate of  $\delta\theta_y(\theta)$ . We then Fourier transform it,  $\delta\theta_y(l) = \int d^2l e^{i\mathbf{l} \cdot \theta} \delta\theta_y(\theta)$ . The dimensionless surface density,  $\kappa(\theta)$ , is given by inverse Fourier transform of

$$\kappa(l) = \frac{-il^2 \delta\theta_y(l)}{l_y}. \quad (8)$$

This inversion is possible for all modes except  $l_y = 0$ . These are long-wavelength modes in the  $y$ -direction that cannot be distinguished from the CMB gradient itself. Hence, the inversion is not unique, although the number of modes for which the inversion fails is small compared to their total number (and becomes a set of measure 0 in the limit of perfect resolution). This degeneracy is similar to the mass-sheet degeneracy, which prevents one from reconstructing  $\kappa$  from ellipticity data for the  $l = 0$  mode. It is more severe here, because there is a whole vector of modes for which the

inversion fails, rather than just a single mode. In the previous section we discussed a particular example of this degeneracy, which prevents one from distinguishing external shear in the direction parallel or perpendicular to the CMB gradient from a constant surface density term. Furthermore, even if  $l_y \neq 0$ , for modes with small  $l_y$  and large  $l_x$  this reconstruction amplifies any noise contribution present in the data, so the final map no longer has uniform noise properties.

### 4. SOURCES OF NOISE

To analyze whether the theoretical predictions above can be detected, we need to compare them to various sources of noise. These sources can be divided into instrumental and astrophysical. Astrophysical sources can arise from Earth's atmosphere, our Galaxy, various cosmological sources along the line of sight, and the cluster itself. They can also arise from gravitational lensing by other objects along the line of sight. Another source of noise is the CMB itself, in the form of its deviation from a pure gradient form assumed in the reconstruction. We can parameterize these sources of noise with their power spectrum, which will characterize the level of fluctuations as a function of scale. This does not contain all the information for a non-Gaussian process, but most of the noise sources that are accumulated along the line of sight will be well approximated as Gaussian because of the projection. Others, such as primary CMB, are believed to be Gaussian already. The most important source of noise that cannot be described with power-spectrum information is emission from the cluster itself, especially SZ and dust. We will discuss these sources of noise in more detail below.

#### 4.1. Signal-to-Noise Ratio Analysis

The total CMB anisotropy can be modeled as

$$\Delta T(\theta) = A g(\theta) + n(\theta), \quad (9)$$

where  $g(\theta)$  is the angular profile of the deflection angle normalized to unity at  $\theta = \theta_s$ . For axisymmetric clusters, its form can be simplified to  $g(\theta) \cos(\phi_\theta)$ , where  $\phi_\theta$  is the azimuthal angle of  $\theta$ . Here  $A$  is a constant that includes both the strength of the cluster and the magnitude of the CMB gradient, while the noise term  $n(\theta)$  denotes all the other contributions to the measurement. They can be parameterized with the power spectrum

$$\langle n(l)n(l') \rangle = C(l) \delta(l - l'). \quad (10)$$

If we have some knowledge of the profile of the cluster deflection angle,  $g(\theta)$ , we can average the temperature over this profile, thus reducing the noise contribution from other sources that do not correlate with the expected profile. We wish to derive the filtering function,  $\Psi(\theta)$ , with which we process the data to obtain an estimate of  $A$ ,

$$\hat{A} = \int \Psi(\theta) \Delta T(\theta) d^2\theta. \quad (11)$$

We can vary the filtering function with respect to the signal-to-noise estimate,  $A/\sigma$ , where

$$\sigma^2 = \langle (A - \hat{A})^2 \rangle = \int |\Psi(l)|^2 C(l) d^2l. \quad (12)$$

It can be easily shown that the optimal filter is  $\Psi(l) \propto g(l)/C(l)$ , and that the variance for this filter is given by

(Haehnelt & Tegmark 1996)

$$\sigma = \left[ \int \frac{|g(l)|^2}{C(l)} d^2l \right]^{-1/2}. \quad (13)$$

If the noise spectrum is white, then the profile of the filter is simply the profile of the deflection angle. This is what one expects, since in that case one is obtaining a positive value. If, however, the noise power spectrum has more power on large (or small) scales, then those large (small) modes are more important to suppress than the small-scale (large-scale) modes. To suppress large-scale modes, one must design a filter that is oscillating, so that its shape cancels the slowly changing mode, while still maximizing the information from the cluster profile. This is what is achieved with the optimal filter above.

For an axisymmetric cluster, the Fourier transform simplifies to

$$g(l) = g(l) \cos \phi_l, \quad g(l) = 2\pi \int \theta g(\theta) J_1(l\theta) d\theta, \quad (14)$$

where  $J_1(x)$  is the Bessel function of first order and  $\phi_l$  is the azimuthal angle of  $l$ . The variance becomes

$$\sigma = \left[ \pi \int \frac{g(l)^2}{C(l)} l dl \right]^{-1/2}. \quad (15)$$

In the examples below, we use the NFW profile for the cluster, observed out to a given radius  $\theta_0$ . We use  $\theta_s = 1.4$  and use various sources of confusion to estimate  $\sigma$ . This can be compared to the expected  $A$  for large clusters, of the order of 5–10  $\mu\text{K}$ , to identify the main sources of noise and the range over which this method could be used to study the clusters.

#### 4.2. Instrument Degradation

The detector adds noise to the signal. This can be parameterized by its power spectrum, which for many instruments can be approximated as a constant,  $C_n(l) = \sigma_n^2 \Omega_p$ , where  $\sigma_n$  is the rms noise at each pixel and  $\Omega_p$  is its solid angle. Current observations of SZ at 30 GHz are reaching noise levels of the order of  $\sigma_n = 15 \mu\text{K}$  at  $1'–2'$  resolution (Carlstrom et al. 1999). This is approaching the level of the signal predicted here, although at these frequencies the dominant signal in the center is coming from the SZ effect. Interferometers are not sensitive to low spatial frequency modes, so one cannot obtain the direction of the gradient from the experiment itself. This must be obtained from a lower resolution experiment, such as MAP. It is possible that the characteristic signature generated by the lensing effect could be observed at larger radii even at these low frequencies, and it would certainly be worthwhile to integrate a few of the clusters down to 5  $\mu\text{K}$  to search for this effect, especially once the direction and the amplitude of the gradient of the CMB are better known. At 217 GHz, which is the zero-crossing frequency for thermal SZ, current observations only reach 100  $\mu\text{K}$  noise per pixel at a similar resolution (Church et al. 1997), dominated by atmosphere noise, discussed below. The next generation of small-scale experiments with larger arrays and longer observation times, such as the Millimeter Interferometer (MINT) or the Arcminute Cosmology Array Receiver (ACBAR), will have sensitivity reaching 5  $\mu\text{K}$  per arcminute-sized pixel in a 100 pixel array over a month of observation and will be more suitable for detecting this effect.

Because of the finite angular resolution of the instrument, the predicted  $\Delta T/T$  must be convolved with the window function of the beam. This dilutes sharp features around the center of the cluster, such as those produced by SIS in Figure 3a. For this case, arcminute resolution would be desirable. For less steep profiles, such as NFW, this is less important. Since the actual signal extends quite far away from the center, even a modest resolution of several arcminutes would still be useful, assuming that other sources of noise discussed below do not dominate the signal. To incorporate the beam dilution into the formalism above, we can replace  $C_n(l)$  with  $C_n(l) \exp[-\theta_b^2 l(l+1)]$ , where  $\theta_b$  is the Gaussian width of the beam. Note that beam dilution does not affect the signal-to-noise ratio if the noise is not dominated by instrument noise.

Applying the noise power spectrum to equation (15), we find that a  $10' \times 10'$  array with 100 pixels, each with 5  $\mu\text{K}$  noise, gives an rms noise of  $\sigma = 1.6 \mu\text{K}$  if the effect of the beam is negligible. For a beam with  $1'$  FWHM, this number increases to 3  $\mu\text{K}$ . Doubling the size of the array or halving the noise per pixel both reduce this number by roughly one-half. These levels of noise are therefore necessary for a positive detection of the effect. Note that doubling the size of the array and keeping the noise per solid angle fixed (equivalent to keeping the observing time fixed) does not significantly change the rms variance. This is because the signal is only slowly dropping off with distance from the center. In this case, changing the FWHM from  $1'$  to  $2'$  makes almost no difference. For the *Planck* 217 GHz channel with 12  $\mu\text{K}$  sensitivity per pixel and  $5'$  FWHM, the noise level is of the order of 10  $\mu\text{K}$ , which is at the detection limits for large clusters. Except for a few exceptional cases, *Planck* will therefore not be able to detect this effect.

#### 4.3. Intrinsic CMB Fluctuations

We have assumed throughout that the CMB can be approximated as a pure gradient. The typical coherence length for the CMB gradient is  $15'$ , and since the lensing effect extends well beyond this scale, this approximation breaks down at large separations from the cluster center. To estimate the level of this contribution, we can use the CMB power spectrum as a source of noise in equation (15). Because the large-scale CMB is approximated as a gradient and removed, we exclude the modes larger than the size of the observed field. The modes smaller than the size of the box cannot be approximated as a gradient, and they contribute noise, which needs to be distinguished from the cluster signal. Without removing the long-wavelength modes with the optimal filter, the rms contribution from the CMB is of the order of 15  $\mu\text{K}$  for a survey of  $10' \times 10'$ , increasing to 100  $\mu\text{K}$  for  $1^\circ \times 1^\circ$ . For such large fields, long-wavelength modes of CMB are a significant source of confusion. This reflects the strongly correlated nature of the CMB on large scales. The optimal filter suppresses the influence of long-wavelength modes by employing alternative positive and negative radial weights. This significantly reduces the long-wavelength modes, while still preserving to a large extent the information about the cluster profile. In this case, the variance decreases significantly, to 4–5  $\mu\text{K}$ . For the *Planck* 217 GHz channel, the total variance remains 10  $\mu\text{K}$ , dominated by the detector noise rather than the CMB. The dominant contribution to the CMB gradient comes from  $l > 500$ , with a 50% contribution coming from  $l > 1000$ . Degree-size fields may thus have a significantly

lower rms CMB gradient than  $10'$  size fields. For large areas, the best strategy is to select fields with a smooth and large gradient across the entire field, thus enhancing the signal and reducing the level of CMB noise.

#### 4.4. SZ Effect from the Cluster

The SZ effect is the dominant signal from clusters in the low-frequency range. It is caused by the scattering of photons by hot electrons in the cluster. The net effect is to increase the energy of photons, and since their number is conserved, this causes their redistribution from the low-frequency Rayleigh-Jeans (RJ) regime into the high-frequency Wiener regime. This creates a deficit of photons and therefore a CMB decrement at low frequencies and an increment at high frequencies, with zero-crossing at 217 GHz. The amplitude of the effect is proportional to the temperature of the cluster and its optical depth. Typical numbers are  $10^8$  K for temperature and 0.01 for optical depth. Positive detections in the RJ tail have by now been achieved for more than 30 clusters with central decrements exceeding 500  $\mu$ K (Carlstrom et al. 1999). This is a huge signal that can easily swamp the lensing signal. However, for an isothermal sphere model, the SZ effect drops off as  $r^{-1}$  in projection, while the deflection angle remains constant. Thus, even if SZ dominates in the centers of the clusters, the lensing effect may nevertheless dominate at larger radii.

To be more quantitative, we can convolve with the optimal filter, which reduces the level of fluctuations and even eliminates them for axisymmetric profiles. Most of the clusters are not axisymmetric, and for reasonable ellipticities the remaining contamination could still be above the expected signal in the center. One can further reduce this contamination by eliminating the central region of the cluster in the analysis. Most of the SZ signal comes from the inner  $1'-2'$  radius, while the lensing signal extends well beyond that. To model the importance of the inner part of the cluster, we repeated the noise analysis excluding the lensing information from the inner  $4'$  region. This increased the variance by 40% and so does not significantly reduce the sensitivity, while reducing the level of the SZ signal by a factor of a few.

Further reduction of this contamination is achieved by observing at 217 GHz. Although this frequency is a zero-crossing for thermal SZ in the nonrelativistic limit, for most of the clusters with large signals, relativistic effects are not negligible. This causes the zero-crossing to scale linearly with the gas temperature (Rephaeli 1995). If the cluster is isothermal and its temperature can be measured from X-ray measurements, then one can correct for this effect. If the cluster is not isothermal, as suggested by recent *ASCA* measurements (Markevitch et al. 1996), then this will induce further fluctuations in the map, which can be at a 10  $\mu$ K level. These fluctuations can be reduced using a lensing filter combined with exclusion of the center, and so do not appear to be a major source of confusion.

#### 4.5. Kinetic SZ Effect from the Cluster

Even if the SZ effect from hot electrons vanishes at 217 GHz, there is another imprint of the CMB photons scattering off cluster electrons, caused by electron bulk motion. This is caused by the Doppler effect, and its magnitude is given by the product of optical depth, typically around

$\tau = 0.01$  in the center, and the radial velocity of electrons in the cluster. The latter is dominated by the bulk motion of the cluster,  $v_r$ , with a typical value of  $v_r = 300$  km s $^{-1}$ . This gives the typical magnitude of the effect in the center at around 30  $\mu$ K, somewhat larger than the lensing signal. Note that the two have the same frequency dependence and cannot be distinguished using this information. However, just as in the case of thermal SZ, kinetic SZ is much more centrally concentrated than the lensing effect. The temperature profile in the presence of both effects is shown in Figure 3d for the case of the NFW profile (we are assuming that gas traces dark matter outside the cluster core). At larger separations from the center, kinetic SZ becomes negligible, because it is sensitive to density times peculiar velocity of the cluster, while the lensing effect remains strong because it is sensitive to the gradient of the gravitational potential, so the two effects can be separated. Excluding the central portion of the cluster and using the optimal filter, we find confusion levels of a few  $\mu$ K.

Another potential source of contamination are the bulk motions within the cluster. If the cluster is not relaxed due to a recent merger, this can produce significant internal motions of the gas (of the order of 500 km s $^{-1}$ ; Haehnelt & Tegmark 1996). The corresponding Doppler effect on the CMB can act as an additional source of fluctuations. Filtering reduces the noise level when the large-scale CMB gradient is known, with the residual contamination at the  $\mu$ K level.

#### 4.6. Sunyaev-Zeldovich and Ostriker-Vishniac Effects along the Line of Sight

In addition to the thermal and kinetic SZ effects from the cluster itself, there is also the contribution from other objects along the line of sight. Kinetic SZ is sometimes divided into a contribution from quasi-linear structures, called the Ostriker-Vishniac (OV) effect, and a contribution from nonlinear structures (kinetic SZ). All of these will be a source of noise uncorrelated with the cluster itself. The magnitude of these contributions is somewhat model dependent. Both can be at a level of a few  $\mu$ K on arcminute scales, with thermal SZ being typically a few times stronger. However, since thermal SZ vanishes at 217 GHz (relativistic corrections are likely to be negligible for smaller halos contributing to the line-of-sight SZ), OV and kinetic SZ effects may be more important as a source of confusion at this frequency. To estimate their effect, we have used the power spectra of thermal SZ as given in Persi, Cen, & Ostriker (1995) and of OV given in Hu (2000). The thermal SZ power spectrum grows roughly proportional to  $l$  and exceeds the CMB around  $l \sim 2000$  at low frequencies. Kinetic SZ is somewhat lower, but also grows at high  $l$  in a similar fashion. Only on intermediate scales do the two exceed the combined CMB and instrument noise power spectrum. Their individual contribution to the lens filter variance varies as a function of angular scale. For the  $5'$  beam with 12  $\mu$ K noise per pixel, the contribution from thermal SZ can double the variance from CMB and noise, making the total 20  $\mu$ K. At this angular resolution, it is necessary to work at 217 GHz frequencies to reduce thermal SZ contamination, although kinetic SZ/OV still increases the variance somewhat. For a  $1'$  beam with 5  $\mu$ K noise per pixel, the contributions from SZ and OV are lower and do not significantly change the rms noise. This is because instrument noise dominates the confusion. Only with a more sensitive detec-

tor would these contributions become important on these scales.

#### 4.7. Dust Emission

Dust emission can arise from three separate sources. First, there is the emission from our own Galaxy. This contribution is fairly smooth, scaling as  $C_l \propto l^{-3}$ , and does not add significant power on small scales. A reasonable estimate for noise variance is  $10 \mu\text{K}$  at  $l = 10$  for the 217 GHz channel (Tegmark et al. 1999), dropping significantly at lower frequencies. Even at 217 GHz, its power spectrum is below the CMB power spectrum everywhere except at very low  $l$ . This foreground is therefore less problematic than the primary CMB, and its inclusion does not significantly change the conclusions given above. As a caution, we should note that this conclusion is based only on the power-spectrum analysis, while dust emission can be strongly non-Gaussian. There are regions where dust emission can be significantly larger than the above analysis would suggest. An example discussed below is in the field of A2163.

Another source of dust emission are the infrared sources along the line of sight. These have been modeled by Toffolatti et al. (1998). The overall contribution from the point sources to the power spectrum depends on the flux limit of the resolved sources. Strong pointlike sources can be removed from the data as outliers, leaving the fluctuations produced by the unresolved sources. These Poisson fluctuations give a white noise power spectrum with rms fluctuations of the order of the flux limit converted to  $\mu\text{K}$  in a beam area times the square root of the number of removed sources per beam area. Adopting conservative modeling, as in Tegmark et al. (1999), we find that at 217 GHz, the rms variance including point sources can reach  $25 \mu\text{K}$  for a  $1'$  beam. This is reduced somewhat at larger angular scales, but there thermal SZ and CMB combined prevent one from reducing the noise below  $10 \mu\text{K}$ . These results indicate that more sophisticated modeling of point sources will be necessary to reduce their contribution to acceptable levels. This can be achieved by using either higher frequencies or higher angular resolution to identify these sources. For example, interferometers can use larger baseline configurations to fully subtract out these point sources.

Finally, there is also the possibility of dust emission from the cluster itself. Such emission could explain recent sub-millimeter observation of A2163 by PRONAOS (Lamarre et al. 1998) and may extend into the 200 GHz range, although an alternative explanation involving Galactic dust is just as likely. This would complicate the assertion that the 217 GHz frequency is the optimal one for identifying this effect. If the cluster dust emission at this frequency is still strong, it may exceed the lensing signal, at least in the center. It seems unlikely, however, that a strong dust component would also be present at larger separations from the center.

#### 4.8. Radio Point Sources

At low frequencies, the main sources of confusion are radio point sources (we here ignore free-free and synchrotron radiation, which typically do not exceed the CMB power spectrum and so are subdominant in contamination). Modeling of these has also been presented in Toffolatti et al. (1998). At 30 GHz, their contribution to the power spectrum using only internal identification (based on their identifica-

tion as outliers in the flux distribution) is about 100 times larger than the point-source contribution from IR sources at 217 GHz. The variance on the filtered profile is around  $100 \mu\text{K}$  for a  $5'$  beam and twice that for a  $1'$  beam. This is of course well known to observers operating in this frequency range, who routinely employ higher sensitivity multi-frequency observations in the same region to eliminate point-source contamination. This can reduce the variance from point sources below the instrument noise,  $15\text{--}40 \mu\text{K}$  for the currently most sensitive experiments (Carlstrom et al. 1999). Again, one can use interferometers with larger baseline configurations to subtract out the point sources. It remains to be seen, however, whether using this additional information can reduce the contamination to the required level of a few  $\mu\text{K}$ .

#### 4.9. Gravitational Lensing

Distortion of the background CMB is caused by all the matter distribution along the line of sight, so there will be additional fluctuations in addition to the effect from the cluster. The effect can be partially modeled by using the lensed instead of an unlensed power spectrum in the estimate of confusion from primary anisotropies discussed above. This gives an additional noise contribution at the level below  $1 \mu\text{K}$ , and so would appear not to significantly contaminate the signal. This approach, however, underestimates this contribution, because the generated CMB power is also correlated with the CMB gradient, and the lens filter does not eliminate it as efficiently as the power spectrum analysis would indicate. As shown in Zaldarriaga & Seljak (1999), lensing along the line of sight primarily generates power on scales smaller than the cluster, with rms amplitude of a few  $\mu\text{K}$ . Averaging over the expected cluster profile reduces this noise to negligible levels compared to other sources.

#### 4.10. Atmosphere Noise

In addition to the sources of noise described above, for ground experiments there is also the atmosphere noise arising from atmosphere temperature (around 15 K) and atmosphere fluctuations. The first can be modeled as a white noise and has properties similar to the instrument noise. For bolometer arrays, it dominates the noise at small scales, so sufficient long integrations are needed to reduce it to acceptable levels. Atmospheric fluctuations are more correlated, and their precise estimate depends on the specifics of the detector, site, weather, etc. They can be reduced significantly using interferometric techniques, and it is expected that they can be reduced to the few  $\mu\text{K}$  levels required.

### 5. CONCLUSIONS

The characteristic signature of a cluster gravitationally lensing a smooth CMB gradient allows one to search for and identify this effect among many other possible sources of fluctuations at small scales. The signal is small, at the level of around  $10 \mu\text{K}$  in the center of the most promising clusters, but changes very slowly away from it. This is in contrast to other sources of anisotropy from the cluster, such as thermal or kinetic SZ, which may exceed this signal in the center of the cluster, but fall off more rapidly away from the cluster center, so that at larger separations the lensing signal becomes dominant.

We have investigated how well noise filtering over the expected profile can reduce the noise contamination. We find that the level achieved is acceptable if the initial guess about the cluster profile is sufficiently close to the real one. The final signal-to-noise ratio depends sensitively on the amplitude of various sources of fluctuations, including instrument noise, all of which are still rather uncertain at present. The most promising among the existing or planned experiments are small-scale interferometers with arcminute resolution and a few  $\mu\text{K}$  noise per pixel, sensitivity operating at frequencies close to 217 GHz. Examples of these are the Cosmic Background Imager (CBI), the Degree Angular Scale Interferometer (DASI), the Very Small Array (VSA), the Atacama Large Millimeter Array (ALMA), ACBAR, MINT, etc. A *Planck* experiment with a  $5'$  beam at 217 GHz could also provide detection in some cases.

Despite the signal being weak, this method of detecting cluster signature has some advantages over the current methods. First, like the SZ effect, the strength does not drop

significantly with redshift, except for the slow decrease from the  $D_{LS}/D_{OS}$  ratio. In addition, the signal depends on the deflection angle, which is more sensitive to the outer parts of the cluster than those probes that depend on the projected density. For the NFW profile, the signal drops by about a factor of 2 between  $\theta_s$  and  $10\theta_s$  (which is beyond the virial radius), while the projected surface density drops by almost 2 orders of magnitude (see Fig. 2). Given that this is one of the few probes sensitive to the outer parts of the cluster, it seems worth pursuing it with the next generation of CMB experiments.

We thank L. Page for useful discussions and the referee, U. Pen, for useful suggestions. M. Z. is supported by NASA through Hubble Fellowship grant HF-01116.01-98A from STScI, operated by AURA, Inc., under NASA contract NAS5-26555. U. S. is supported by NASA grant NAG5-8084.

#### REFERENCES

- Carlstrom, J. E., et al. 1999, preprint (astro-ph/9905255)  
 Church, S. E., et al. 1997, *ApJ*, 484, 523  
 Haehnelt, M. G., & Tegmark, M. 1996, *MNRAS*, 279, 545  
 Hu, W. 2000, *ApJ*, 529, 12  
 Lamarre, J. M., et al. 1998, *ApJ*, 507, L5  
 Markevitch, M., et al. 1996, *ApJ*, 456, 437  
 Mellier, Y. 1999, *ARA&A*, 37, 127  
 Navarro, J. F., Frenk, C. S., & White, S. D. M. 1997, *ApJ*, 490, 493  
 Persi, F. M., Cen, R., & Ostriker, J. P. 1995, *ApJ*, 442, 1  
 Rephaeli, Y. 1995, *ARA&A*, 33, 541  
 Tegmark, M., Eisenstein, D., Hu, W., & De Oliveira-Costa, A. 2000, *ApJ*, 530, 133  
 Toffolatti, M., et al. 1998, *MNRAS*, 297, 117  
 Williams, L. L. R., Navarro, J. F., & Bartelmann, M. 1999, *ApJ*, 527, 535  
 Zaldarriaga M. 1999, preprint (astro-ph/9910498)  
 Zaldarriaga M., & Seljak, U. 1999, *Phys. Rev. D*, 59, 123507